ChemComm

Colloidal Ag_2Se Intraband Quantum Dots

Journal:	*ChemComm*
Manuscript ID	CC-FEA-05-2023-002203.R1
Article Type:	Feature Article

FEATURE ARTICLE

Colloidal Ag_2Se Intraband Quantum Dots

Mohammad Mostafa Al Mahfuz,[a] Junsung Park,[a] Rakina Islam,[a] and Dong-Kyun Ko*[a]

Received 00th January 20xx,
Accepted 00th January 20xx

DOI: 10.1039/x0xx00000x

With the emergence of Internet of Things, wearable electronics, and machine vision, the exponentially growing demands in the miniaturization, energy efficiency, and cost-effectiveness have imposed critical requirements on the size, weight, power consumption and cost (SWaP-C) of infrared detectors. To meet this demand, new sensor technologies that can reduce the fabrication cost associated with semiconductor epitaxy and remove the stringent requirement for cryogenic cooling are under active investigations. In the technologically important spectral region of mid-wavelenghth infrared, intraband colloidal quantum dots are currently at the forefront of this endeavor, with wafer-scale monolithic integration and Auger suppression being the key materials capabilities to minimize the sensor's SWaP-C. In this Feature Article, we provide a focused review on the development of sensors based on Ag_2Se intraband colloidal quantum dots, a heavy metal-free colloidal nanomaterial, that has merits for wide-scale adoption in consumer and industrial sectors.

1. Introduction

The reduction in materials dimensionality confines electrons and holes to a small space. When the length of the semiconductor material in one of the dimensions is reduced down to the scale of the de Broglie wavelength of charge carriers, quantum confinement effect takes place. This gives rise to evolution of discrete and quantized energy levels that are different from the continuous energy band formed in bulk. This fundamental principle was first exploited to create one-dimensionally confined nanostructures, known as quantum wells (QWs), and was further developed toward 2-D quantum wires, and 3-D quantum dots. Colloidal quantum dots (CQDs) represent a unique class of three-dimensionally confined semiconductor nanomaterial that have diameters typically less than 10 nm and are coated with surface ligands that facilitate stable colloidal dispersion in variety of solvents.[1]Harnessing the interband transition in these quantum confined nanostructures has been the mainstream theme in semiconductor research. Interband transition refers to a process where carrier excitations or relaxations occur between the quantized electronic states between the lowest unoccupied conduction level and highest occupied valence level. More unique optoelectronic properties can be harnessed by utilizing the transitions within the conduction levels or valence levels, known as intersubband (intraband) transition.[2] In fact, intersubband optical transitions in QWs, have a long and successful history.[3] Since the initial observation of intersubband optical absorption in a GaAs QW structure, substantial research and development efforts have led to promising new device concepts, two most important examples being quantum well infrared photodetectors (QWIPs)[4,5] and quantum cascade lasers (QCLs).[6] QWIPs and QCLs are fabricated from well-established III-V molecular beam epitaxy which offers excellent interfacial abruptness, thickness control, and chemical as well as structural uniformity. In particular, InGaAs/InAlAs QWIPs and GaAs/AlGaAs QCLs operating in the mid-wavelength infrared (MWIR = 3 – 5 μm) spectral region have reached a competitive level of performance and the continuous technology maturation has led to many commercial products that are available today. Notably, the QCL research has undoubtedly become the most impressive field of intersubband optoelectronics, enabling MWIR lasers capable of continuous-wave operation at room temperature[7,8] and establishing a major milestone of extending the laser wavelength toward the terahertz regime.[9,10]

While the observation of intersubband optical transition in colloidal quantum dots (CQDs) dates back as far as 1998,[11] CQD optoelectronic devices have remained exclusively as interband devices. With the emergence of chemically-stable n-doped CQDs, intersubband optoelectronics applications have recently become feasible.[12–15] A typical n-type intraband CQD has electrons doped up to the first quantum confined energy levels ($1S_e$) and utilizes the optical transitions between $1S_e$ and the second ($1P_e$) quantum confined energy levels. Two primary features of intraband CQDs are: (1) the ability to access the infrared spectral regions of longer wavelength, including MWIR, long-wavelength infrared (LWIR = 9 – 12 μm), and up to terahertz;[16,17] and (2) the Auger suppression property[18] that can potentially allow high-sensitivity operation of infrared detectors without cryogenic cooling. Since the quantum confinement only allows the CQDs to have an energy gap larger than the material's bulk bandgap, the smallest energy gap achievable in CQDs was limited by the bulk bandgap. By utilizing the intraband transition, the constraint arising from the bulk bandgap limit is therefore removed, allowing access to longer wavelength regions beyond the near infrared.[19,20] Furthermore,

[a] Department of Electrical and Computer Engineering, New Jersey Institute of Technology, Newark, New Jersey 07102, United States. Email: dkko@njit.edu

Auger recombination process which is a major obstacle that prevents narrow bandgap semiconductor detectors from reaching high sensitivity without cryogenic cooling,[21,22] is significantly reduced in intraband CQDs. In HgSe intraband CQDs, as a specific example, the Auger coefficient has been reported to be three orders of magnitude lower compared to that of the bulk counterpart due to the suppression of hole recombination pathway.[18] This Auger suppression property can allow high sensitivity, uncooled MWIR photodetection, similar to polycrystalline lead salt (PbSe) detectors.[23]

Intraband CQD technology is expected to bring a significant impact, especially in the field of MWIR sensing which is currently dominated by expensive, cryogenically-cooled epitaxial semiconductor devices. While MWIR detectors have been traditionally used for military surveillance, dominant future demands are anticipated to be sensors for autonomous vehicles, drone and microsatellite mounts, robotic vision and advanced augmented goggles, of which size, weight, power consumption and cost (SWaP-C) becomes a key criterion.[24] High cost of device-quality material growth, complexity of focal plane array fabrication (flip-chip bonding[21]), and the need for bulky, heavy, high-power consuming cryocoolers make epitaxial devices unsuitable for many emerging applications. The current demand for low-cost, uncooled detector options in the thermal infrared is thereby entirely met by microbolometers. However, microbolometers are optimized for LWIR detection[25,26] hence perform poorly in the MWIR,[25,27] and this presents a technology gap.[28,29] Detectors based on intraband CQDs have the potential to position themselves as a viable low SWaP-C option to fill this MWIR technology gap. The low cost and reduced cooling requirement are enabled by the inexpensive method of producing a large volume of CQDs, the availability of monolithic device fabrication using wafer-scale solution processing, and intraband CQD's unique Auger suppression properties.

For MWIR detector applications, electron doping in intraband colloidal quantum dots must be chemically stable, so as to allow steady-state access to intraband optical transition and to enable applications as solid-state devices. Currently, available materials options are HgSe CQD – a performance-leading colloidal nanomaterial,[16,30,31] Ag_2Se CQD – the sole non-toxic alternative intraband material,[24,32] and recently reported PbS CQD.[19,33] In this Feature Article, we provide a focused review on the current progress, challenges, and future prospects of Ag_2Se CQD-based MWIR detectors. Compared to Cd-, Pb-, or Hg-chalcogenide CQDs that have a long track record of research, Ag_2Se CQDs are free of heavy metals, making them suitable for ubiquitous use in many application areas with minimal health and environmental concerns. We start with the review of the synthesis and characterization of Ag_2Se CQDs, examine the fabrication and performance characterization of various detector device structures, discuss the opportunities and challenges compared to the state-of-the-art, and conclude with the future outlook of this technology.

2. Silver selenide (Ag_2Se)

Silver selenide (Ag_2Se) belongs to a relatively less explored, group I-VI compounds semiconductor family. Bulk orthorhombic Ag_2Se at room temperature, possess a narrow, direct band gap of 0.15 eV[34]and has attracted considerable attention in the recent years as a promising thermoelectric material, owing to its high carrier mobility (~ 1500 cm^2/V s) and low thermal conductivity (~ 1.3 W/mK).[35] In a CQD form, ultrasmall (sub-3nm), water-dispersible Ag_2Se CQD (interband) are under active investigation for bio-imaging agent due to their excellent fluorescent property in the near-infrared window, high penetration to biological membranes and tissues, and reduced toxicity.[36,37]

Ag_2Se is traditionally not a known infrared semiconductor device material. When Ag_2Se CQDs are grown to larger than 5.0 nm in diameter, CQDs become n-doped (due to environmental Fermi level doping mechanism, as discussed in more detail in section 4), allowing the access to intraband $1S_e$-$1P_e$ optical transition. The solution-based device fabrication enabled by the colloidal nature of the CQDs and the unique MWIR photophysical properties offered by intraband character makes Ag_2Se CQDs a technologically interesting materials platform for infrared sensor development.

3. Colloidal synthesis of Ag_2Se CQDs

Preparing CQDs with uniform size and shape is a prerequisite to fabricating high performance CQD-based infrared sensors. Earlier efforts to synthesize Ag_2Se CQDs include chemical transformation of Ag metal nanocrystals[38] positive microemulsion, and double jet precipitation[39], which showed limited control over size and shape. The first demonstration of monodispersed, spherical Ag_2Se CQDs synthesis was reported by Sahu et al.[40] The synthesis was based on hot-injection[41] of trioctylphosphine silver (TOP-Ag) and trioctylphosphine selenide (TOP-Se) into trioctylphosphine oxide (TOPO), of which TOPO serves both as a ligand and a solvent. This method was later adapted to a more convenient ligand-solvent system, oleylamine, which stays in a liquid phase at room temperature. A standard synthesis protocol (Fig. 1) starts with preparing TOP-Ag and TOP-Se precursors by dissolving AgCl and Se powder in trioctylphosphine (TOP), respectively, in an inert environment. Then, in a reaction vessel, oleylamine is heated to 90 °C under a vacuum for 1 hour. Next, Se precursor (TOP-Se) first is injected into the degassed oleylamine and the mixture is heated to a

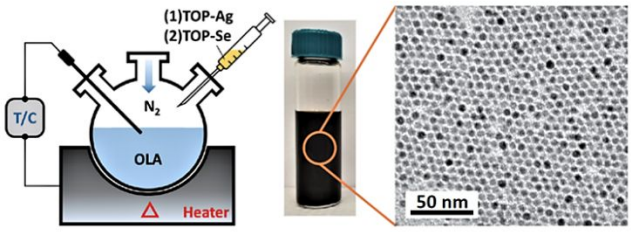

Fig. 1 Schematic diagram of Ag_2Se colloidal synthesis, sample CQD solution, and a corresponding TEM image of CQDs.[15] Copyright © 2019 American Chemical Society

desired reaction temperature under nitrogen. After the mixture reaches the desired temperature, TOP-Ag solution is rapidly injected into the reaction vessel, forming a dark solution. The reaction is then terminated by injecting butanol and quenching the reaction vessel in a water bath. Finally, synthesized CQDs are purified using a solvent/anti-solvent combination. Ag_2Se CQDs of various diameters, ranging from 5.5 nm to 9.2 nm, were synthesized, by adjusting the reaction temperature and growth time (5.5 - 6.5 nm), changing the precursor concentration ratio of TOP-Ag and TOP-Se (6.5 - 8nm) and conducting regrowth by the introduction of additional precursors (> 8nm).[17] The intraband absorption peak of these CQDs cover the infrared spectrum ranging from 4.0 to 8.0 µm.

One drawback of this synthesis recipe is the low synthetic yield (typically less than 3 mg for 25 mL volume reaction for QDs of sizes smaller than 5.5 nm).[42] While the fabrication of planar photoconductive devices typically requires a small quantity of CQD solution, advanced vertically-stacked devices usually require larger CQD quantities to complete more than 20 layers of CQD film deposition. Hence, increasing the CQD synthetic yield became imperative for further device development. Previous studies revealed that pure tertiary phosphine chalcogenides, such as TOP-Se used in the synthesis, were rather unreactive to metal precursors.[43] Instead, the secondary phosphines, typically present as impurities in tertiary phosphine products, are entirely responsible for the nucleation of QDs. Hence, it has been reported[42,43] that a small addition of secondary phosphines, such as diphenylphosphine (DPP), can dramatically increase the synthetic yield. Following this synthetic strategy, Hafiz et al.[42] reported a 10-fold increase in 5.5 nm Ag_2Se QD synthesis yield (50 mg for 55 mL volume reaction) without sacrificing the QD size uniformity, by adding a small amount of DPP (TOP/DPP = 30:1 in volume) in the reaction.

Different metal precursor sources, other than TOP-Ag, were also reported for the Ag_2Se colloidal synthesis.[20,38,44] Notably, highly monodispersed Ag_2Se CQDs were reported by Son et al.[44] (Fig. 2) which used $AgNO_3$ dissolved in oleylamine as an Ag source. Recently, preparation of Ag_2Se CQDs through the cation exchange of PbSe CQDs was reported.[45] These CQDs exhibit stable intraband transition energies above 0.39 eV (absorption peak below 3.3 µm), which was previously difficult to access using hot-injection synthesis.

Due to the increasing interest in the intraband CQDs in the recent years,[46–48]reports on the colloidal synthesis of Ag_2Se CQDs are on the rise.[20,38,44]However, compared to traditional Cd- and Pb-chalcogenide CQDs, understandings on the nucleation and growth is still lacking. Especially, systematic studies on the CQD growth kinetics[49–51] and investigating new precursors that have optimal reactivity[52,53] can help to advance the colloidal synthesis of Ag_2Se CQDs. Also, mass production route to obtaining high quality CQDs, such as continuous flow synthesis,[54,55] has not yet been applied to Ag_2Se CQDs, leaving a large space to be explored in the future.

Surface capping ligands are the critical component of the CQD material system. Surface ligands help CQDs to sustain colloidal suspension and promote surface defect passivation. They also dictate many important parameters of the CQD film such as photoluminescence quantum yield, carrier mobility and lifetime, doping, and energy level position. For optoelectronic device applications, the ligands used during the synthesis are replace with smaller molecules, ethanedithiol (EDT) being the prominent one for Ag_2Se CQDs, and are discussed in more detail in the sections 6 and 8.

4. Structural characterization of Ag_2Se CQDs

The high surface energy plays a critical role in determining the total Gibbs free energy of a CQD system, making it feasible to attain thermodynamically stable crystal structures that are typically metastable in bulk.[56–59] One such example is evident in the case of Ag_2Se CQDs. In bulk, Ag_2Se exhibits orthorhombic(β-Ag_2Se) structure[60,61] having a narrowband gap (0.15eV).[34] When Ag_2Se is synthesized into nanometer-sized crystallites, below a nominal size of 40 nm,[62] they exhibit a crystal phase different from the bulk.[44,45,63–65] The exact crystal structure of the Ag_2Se CQDs has been a topic of debate; the precise determination of phase identity is typically hindered by the Scherrer broadening in the X-ray diffraction (XRD) analysis and the presence of different capping ligands used in the synthesis that can alter the

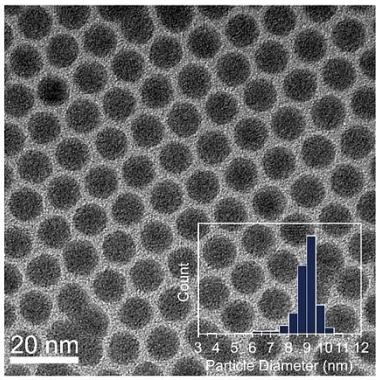

Fig. 2 TEM image of oleylamine-passivated Ag2Se CQDs with narrow size distribution.[44] Copyright © 2020 American Chemical Society

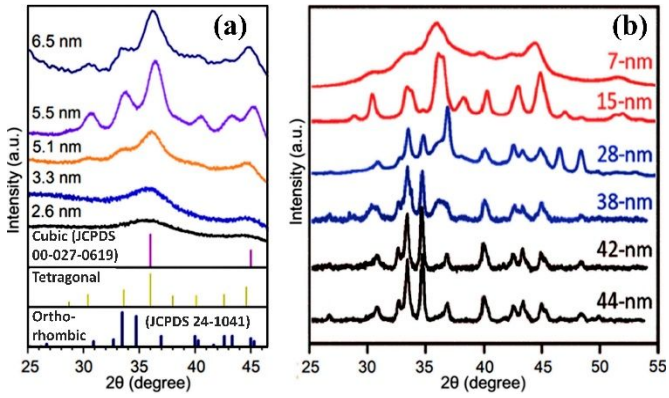

Fig. 3 (a) XRD data obtained from Ag_2Se CQDs with varying sizes.[20] Copyright © 2021 American Chemical Society (b) XRD data showing a transition from tetragonal phase to orthorhombic phase with increasing grain size.[62] Copyright © 2013 American Chemical Society

thermodynamic stability of the room-temperature crystal phase.[66–68] Scimeca et al.[20] studied the crystal structures of DDT-ligand capped Ag_2Se CQDs with sizes varying from 2.6 nm to 6.5 nm (Fig. 3(a)). Combined XRD and high-resolution transmission electron microscopy (HRTEM) analyses revealed a tetragonal crystal structure (t-Ag_2Se). By enlarging the grain size through controlled sintering, it was also found that t-Ag_2Se CQDs transform into bulk β-Ag_2Se at a size around 40 nm (Fig. 3(b)).[62,68] Sahu et al.[62] also demonstrated a reversible phase transition (t-Ag_2Se to α-Ag_2Se and vice versa) of 8.6 nm CQDs via conducting heating and cooling cycles. On the other hand, Son et al.[44] reported the identification of both cubic(α-Ag_2Se) and tetragonal structures in oleylamine-capped Ag_2Se CQDs. While the smaller CQDs (~ 4.8 nm) are composed of cubic crystal structure (α-Ag_2Se), with the increasing CQD size, t-Ag_2Se phase was observed. Tappan et al.[65] conducted a detailed XRD analysis using Rietveld refinements (Fig. 4(a)). Polyvinylpyrrolidone-capped, oleylamine-capped, and N-heterocyclic carbene-capped Ag_2Se CQDs with sizes corresponding to 143 nm, 55 nm and 26 nm, respectively, were synthesized using solvothermal synthesis. These large Ag_2Se nanoparticles all exhibited anti-$PbCl_2$-like structure (Fig. 4c) and the density functional theory (DFT) calculation shows that it is a semiconductor with a narrow band gap of 0.13 eV. Compared to the tetragonal structure (Fig. 4(b)) which has a slightly distorted face-centered cubic lattice of Se^{2-} anions containing Ag^+ cations, the reported anti-$PbCl_2$-like structure has a distorted edge sharing $AgSe_4$ tetrahedra, featuring monoclinic with space group $P2_1/n$.

The study of crystal structure also shines a new light on the understanding of synthetic mechanism of Ag_2Se CQDs. The temperature usually used for Ag_2Se synthesis[15,42,62,68] is higher than the $t \rightarrow \alpha$ transition temperature of Ag_2Se CQDs (101–109 °C).[62,67–69] It was discussed that under these synthetic temperatures, Ag_2Se first crystallizes in an α-Ag_2Se phase first and transforms later into a t-Ag_2Se during the reaction cool down.[44] Wang et. al.[68] hypothesized that this may play a role in narrowing the size distribution of Ag_2Se CQD during the synthesis as the cubic to tetragonal phase transition can help constrain the size of the as-synthesized nanomaterials.[62,67,70–72]

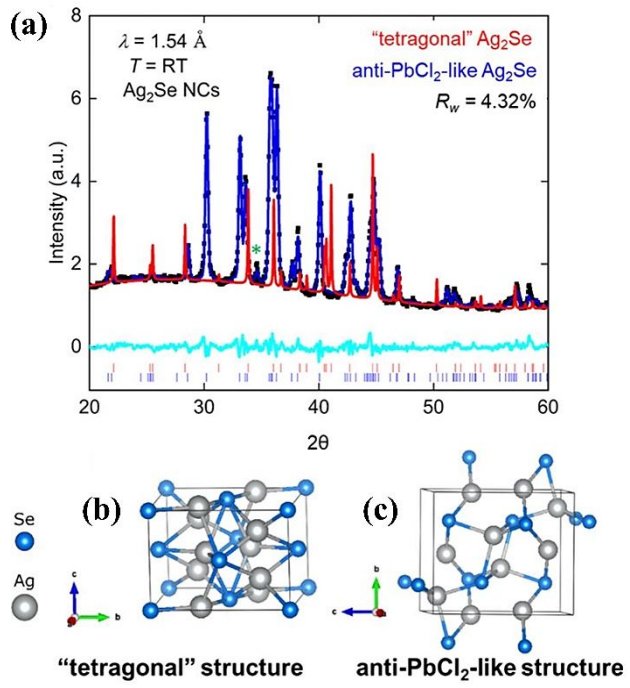

Fig. 4 (a) Plot of experimental XRD data of Ag_2Se CQDs (black), Rietveld refinement model (blue), and the difference pattern (turquoise). Tetragonal phase reported by Günter and Keusch (red) is overlayed in the same graph. (b) Günter and Keusch's tetragonal phase unit cell. (c) anti-$PbCl_2$-like polymorph Ag_2Se unit cell.[65] Copyright © 2021 American Chemical Society

Crystal structures govern many fundamental properties of the material. Parameters such as interband/intraband energy gap, energy level splitting, and their temperature dependencies[44]which are important for infrared sensor development can be predicted by computational modelling based on nanomaterial's crystal structure. Yet, there are widely dispersed reports on structural identification of MWIR intraband Ag_2Se CQDs; there are several reports of XRD studies focused on different size regimes and the CQD synthesis methods as well as the final surface capping ligands vary widely. While it is understood that Ag_2Se CQDs show crystal structure clearly different from that of the room temperature bulk orthorhombic phase (β-Ag_2Se), the exact structure has not been determined experimentally. This issue is compounded by the fact that a standard synthetic protocol has not been established for Ag_2Se CQDs to date. A dedicated synthesis and structure characterization combinatorial studies are required to further illuminate this.

5. Optical properties of Ag_2Se intraband CQDs

While there are many literature reports on the small Ag_2Se CQDs (less than ~ 3nm) that exhibit interband optical absorption in the near-infrared[20,73,74] and large Ag_2Se CQDs (higher than ~ 6 nm) that show the emergence of plasmonic resonance due to the splitting of $1P_e$ level,[44] we focused on Ag_2Se CQDs in the mid-size range that allows intraband absorption in the technologically important spectral region of MWIR in the 3 - 5 µm. In these size ranges, optical transitions occur between the first ($1S_e$) and the second ($1P_e$) quantum confined energy levels. The optical gap of $1S_e - 1P_e$ can be varied through controlling the CQD size similar to the traditional interband CQDs, and their absorption peak can span a wide range in the MWIR as shown in Fig. 5(a). The basic optical transition pathways suggests that the electron population of two-fold degenerate $1S_e$ level[75] should strongly modulate the strength of the intraband versus interband absorption in Ag_2Se CQDs. This was first studied by Park et al.[14] using spectroelectrochemistry (SEC) measurement system which can dope or de-dope the $1S_e$ of Ag_2Se CQDs by applying reduction (electron addition) or oxidation (electron withdrawal) electrochemical potentials. As shown in Fig. 5(b), under negative electrochemical potential, the absorption MWIR (2201 cm^{-1}, intraband) gained strength while the absorption at the shorter wavelength (5485 cm^{-1}, interband) was bleached.

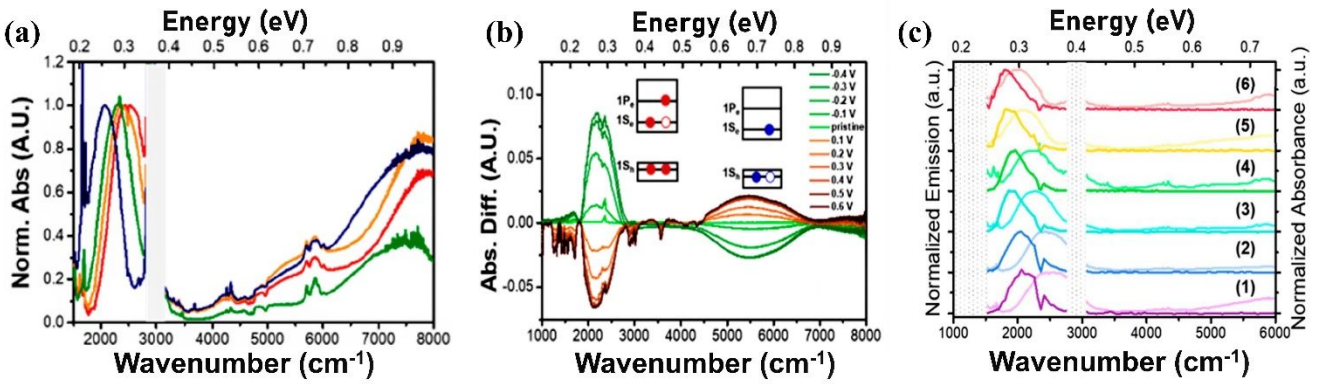

Fig. 5 (a) Optical absorption measurement of Ag_2Se CQDs with varying sizes using Fourier transform infrared (FTIR) spectroscopy. (b) Differential absorption spectra of Ag_2Se nanocrystals with positive (red) and negative (green) electrochemical potentials. (c) PL spectrum of Ag_2Se CQDs of different size plotted with absorbance.[14] Copyright © 2018 American Chemical Society

Conversely, an opposite effect was observed when a positive electrochemical potential was applied. Room-temperature photoluminescence (PL) was also observed for these Ag_2Se CQDs (Fig. 5(c)), which confirms that the optical absorption in the MWIR is intraband transition in nature rather than localized surface plasmon resonance (LSPR).[76]

Interestingly, Ag_2Se CQDs synthesized from hot-injection synthesis show a peculiar optical trend as a function of growing CQD size. The intraband absorption peak abruptly emerges at 4.0 µm at a size around 5.0 nm, and continues to redshift with increasing CQD size.[14,17,44] However, below this size, the MWIR peak is not observed. This phenomenon is understood based on the environmental Fermi level (EFL) doping mechanism[20,77]. In this mechanism, as the CQD size grows larger, the energy gap of the CQDs gets smaller, thereby pushing the $1S_e$ below the EFL, as shown in Fig. 6. Since the EFL position is higher than $1S_e$, the CQDs are electrochemically reduced (electrons added), hence allowing the MWIR intraband transitions. This mechanism suggests that there is a specific size at which the Ag_2Se CQDs start to exhibit intraband character, explaining the observed phenomenon. However, a recent synthesis report of cation-exchanged Ag_2Se CQDs has shown that CQDs with sizes smaller than 5 nm do show stable intraband transition where the MWIR absorption peak lies below 3.3 µm.[45] This can be attributed to different surface ligands (oleic acid and oleylamine) that induce dipoles that can shift the entire energy levels with respect to the reference vacuum level,[78,79] while further investigation is warranted to fully understand the phenomenon.

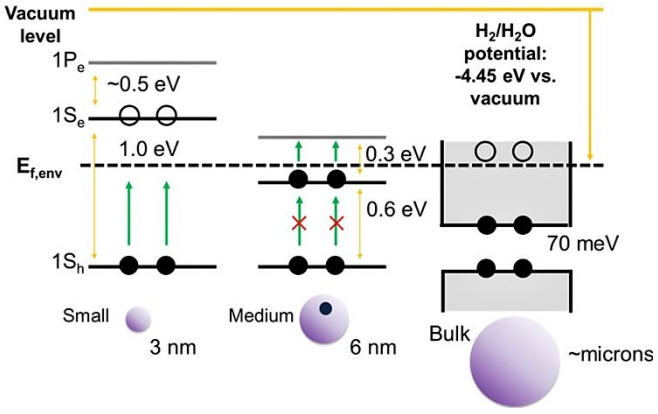

Fig. 6 Schematic illustrating the environmental Fermi level (EFL) doping mechanism and its dependence on particle size. Smaller Ag_2Se has a vacant $1S_e$ level due to strong confinement that shifts the 1Se level above the EFL. Increasing the particle size relaxes quantum confinement, causing the $1S_e$ level to drop below the EFL and become occupied by electrons.[20] Copyright © 2021 American Chemical Society

The absorption coefficient is a measure of how strongly a material with a given thickness absorbs the light (infrared radiation) and provides the first clue as to whether the material is suitable for optical sensor applications. A study conducted by Hafiz et al.[80] showed that a thin-film deposited from EDT ligand-exchanged Ag_2Se CQDs have an absorption coefficient of $(9.5 \pm 0.5) \times 10^3$ cm^{-1} at 5 µm peak, a value comparable to the leading research MWIR CQD material, HgTe[81], and bulk single-crystalline HgCdTe films which is considered as a golden standard material for MWIR.[82] Various optical studies discussed in this section suggests that Ag_2Se CQDs are a promising MWIR absorber material for sensor devices. The colloidal nature of Ag_2Se CQDs provide a unique advantage over current state-of-the-art epitaxial devices, allowing low-cost solution-based fabrication of which solution-processable materials options are rare in the MWIR spectral region.

6. Electrical properties of Ag_2Se intraband CQDs

As-synthesized CQDs have long capping ligands attached to the surface which enables the colloidal stability but impedes the charge transport. For optoelectronic applications, the native capping molecules are ligand-exchanged to compact, shorter ones which drastically improves the electrical conductivity due to reduced interdot distance that facilitates greater electron wavefunction overlap.[83] Majority of the device studies are currently based on EDT ligand-exchanged Ag_2Se CQD films and hence are examined in this section.

Understanding the position of conduction and valence energy levels are prerequisite to the device design. Fig. 7 shows the X-ray photoelectron spectroscopy (XPS) measurement of EDT ligand-exchanged Ag_2Se CQD films.[64] As shown in Fig. 7(a), the cut off at the high binding energy of the XPS spectrum reveals the position of the Fermi energy level (E_F), which lies in

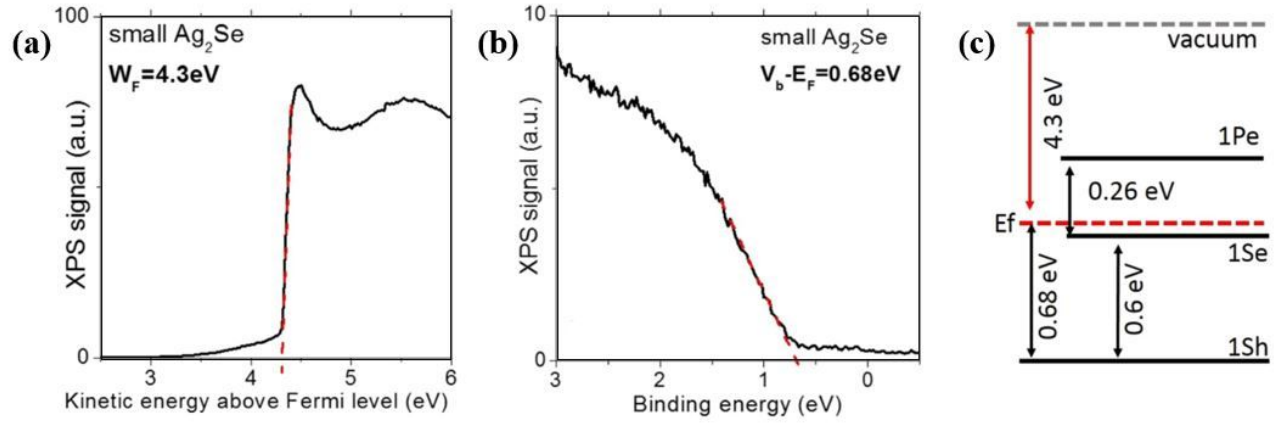

Fig. 7 XPS spectrum near (a) high energy cut off and (b) low energy cut off. (c) Positions of energy levels of EDT-ligand exchanged Ag_2Se CQD film plotted with reference to the vacuum level.[50] Copyright © 2018 American Chemical Society

between the $1S_e$ and $1P_e$ level, in agreement with the intraband character of the CQD film. The position of the $1S_h$ is estimated from the cut off in the low energy binding part of the spectrum (Fig. 7(b)) and the positions of the $1S_e$ and $1P_e$ are determined from the interband and intraband optical gaps, respectively (Fig. 7(c)). Temperature-dependent conductivity (under dark, Fig. 8(a)) reported by Qu et al.[64] also agrees with the XPS analysis. The thermal activation energy extracted from 300 – 200 K temperature range is 164 meV, which is a close agreement with the energy difference between the $1P_e$ (conduction level for n-type intraband CQD) and E_F of 180 meV shown in Fig. 7(c).

In CQD research field, field-effect transistor (FET) measurements are widely used to understand the carrier transport properties because the Hall measurements are not adequate for hopping conduction material like CQD films.[80] Hafiz et al.[17] studied the transfer characteristics of a conventional bottom-gate/top-contact field-effect transistor fabricated from EDT-ligand exchanged Ag_2Se CQD film. The minimal gate response and rising drain current with increased gate bias suggest that the sample film is degenerately-doped n-type. More details are revealed through top electrolyte-gated transistor measurement reported by Qu et al. (Fig. 8(b)).[64] Increasing drain current with increasing positive gate bias again indicates the n-type semiconductor character of the CQD film. The observed negative threshold voltage (depletion mode of operation) and low on/off ratio also reflect the heavily-doped nature of the CQD film. The Seebeck measurement reported by Hafiz et al.[15] also directly corroborates this n-type intraband nature of the CQDs. The negative sign of the Seebeck voltage directly reveals the majority carrier as n-type, and the small magnitude of the Seebeck coefficient is an indicative of degenerately-doped nature of the intraband CQD film.

While there is no report on the carrier mobility values of EDT ligand-exchanged Ag_2Se CQDs, CQD films in the thermally-activated hopping regime typically exhibit low mobility below 0.1 $cm^2/V{\cdot}s$.[84]This is anticipated to be the greatest challenge for achieving high performance CQD sensors. Regardless of the device type (photoconductors or photodiodes), all photosenors follow three fundamental steps of device operation: (1) light absorption, (2) charge separation, and (3) charge collection.[24] The low carrier mobility of CQD films will primarily affect the efficiency of carrier collection thereby degrading the photocurrent magnitude that determines the device responsivity and external quantum efficiency (EQE). Tackling this challenge lies in identifying ligands that maximize the carrier mobility, as we discuss in more detail in the conclusion section of this feature article. Recent bulk-like mobility observed in well-designed CQD-ligand systems[85,86] highlights a

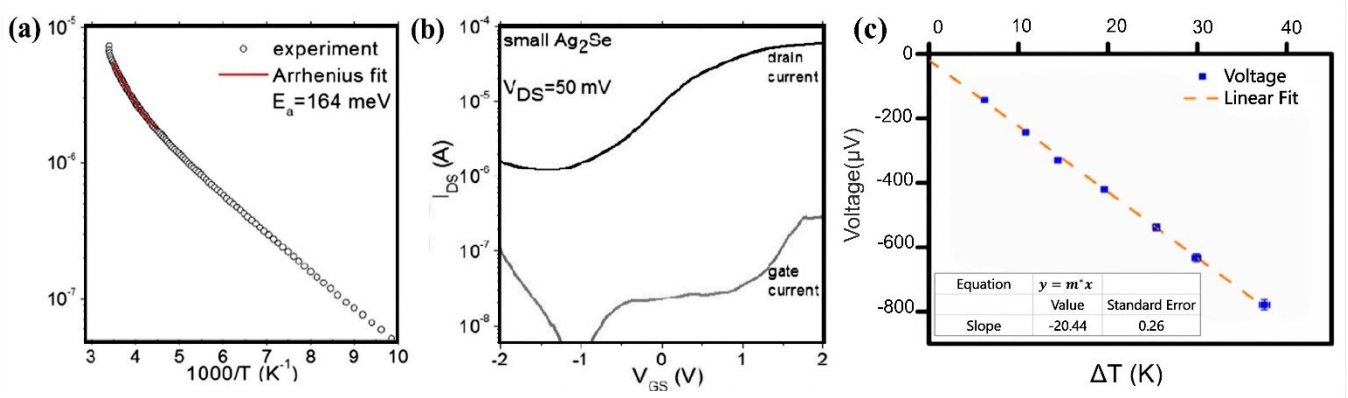

Fig. 8 (a) Temperature-dependent conductivity plot obtained from EDT ligand-exchanged Ag_2Se CQD film.[64] (b) Transfer characteristic of an electrolyte-gated FET.[64] Copyright © 2018 American Chemical Society (c) Seebeck measurement (open-circuit voltage vs. temperature difference) of EDT-treated Ag_2Se CQD film.[15] Copyright © 2019 American Chemical Society

possible future direction toward improvements in carrier transport properties.

7. Device fabrication and performance characterization of MWIR detectors

7.1 Photoconductive devices

To examine the potential of intraband Ag_2Se CQDs for MWIR sensors, an initial device study based on planar photoconductive photodetectors was conducted.[15,17] The devices were fabricated by drop-casting 5.0 – 5.5 nm Ag_2Se CQDs (intraband peak at 4.0 – 4.5 µm) on Si/SiO_2 substrates that are pre-patterned with Cr/Au interdigitated electrodes (channel length: 10 µm, total width: 64.9 mm) formed by photolithography. The CQD film is then ligand-exchanged with EDT to increase the electronic coupling between CQDs. Three to four cycles of layer-by-layer (LBL) CQD deposition and ligand-exchange is conducted to form 70 ± 10 nm thick absorber film. CQD films deposited outside the sensor area were removed to complete the device. A typical device is depicted in Figure 9(a). This two-terminal photoconductive cell represents the simplest sensor device structure where a light-sensitive semiconductor is deposited directly on top of two Ohmic contact electrodes that are separated by a known distance.

The spectral responsivity measurement was conducted using calibrated blackbody heated at 900 °C as an infrared radiation source. This illumination source is modulated using an optical chopper and a set of Fabry–Perot band-pass filters with the center wavelength varying from 2 – 7 µm was used for spectral discrimination. Photocurrents were measured using SR830 lock-in amplified coupled with SR570 preamplifier. The responsivity is calculated by dividing the measured photocurrent with the optical power estimated for each center wavelength that was corrected for source aperture size, optical path length, absorption from optical components, and detector area. The advantage of this measurement method is that it enables the measurement of absolute responsivity values at each spectral data points, compared to FTIR-assisted photocurrent characterization methods[16,87] which outputs relative values. Fig. 9(b) shows the room-temperature spectral responsivity of the photoconductive device. With increasing bias, increasing the responsivity with a peak at 4µm was observed. Increasing the bias enhances the charge separation and collection of photogenerated carriers, which results in increases in the photocurrent and responsivity values. The device responsivity can be further increased by applying a higher bias. Yet, the device suffers from materials instability (due to mobile silver ions) and applying a bias higher than 0.3 V induces irreversible degradation to the device. The spectral shape of the device's response coincides with the optical absorption spectrum obtained from Ag_2Se CQD film, indicating that Ag_2Se CQDs are responsible for the observed MWIR responsivity. As a note, responses arising thermal (bolometric) effect would not show spectral discrimination and is expected to exhibit a broad response across the entire infrared spectral region, which is not observed here. Other photoconductive device studies were reported by Qu et al.[64] where 4.4 µm quantum cascade laser (QCL) was used as a light source and by Bera et al.[45] which studies the first Ag_2Se CQD films having intraband peak below 4 µm.

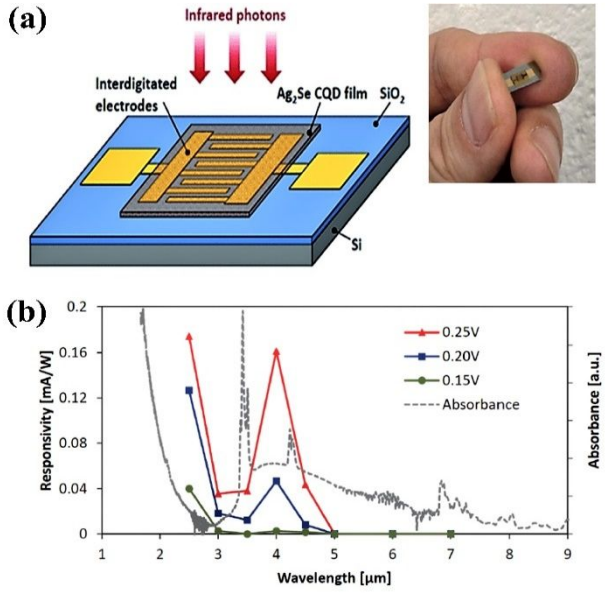

Fig. 9 (a) Planar photoconductive device made from Ag_2Se intraband CQDs.[15] Copyright © 2019 American Chemical Society (b) Spectral response obtained from the same device. The optical absorption of the Ag_2Se CQD film is overlaid for comparison.[17] Copyright © 2019 ECS - The Electrochemical Society

Despite low responsivity values, the observation of photoconductive response from Ag_2Se CQD films without cooling is an intriguing result, which attests the feasibility of Ag_2Se CQDs for MWIR sensor applications. The device's responsivity can be further improved by shortening the electrode distance. The 10 µm channel gap defined here significantly reduces the charge collection efficiency, as the carrier diffusion length in a typical CQD film is less than 300 nm.[88,89] Hence, adopting a vertically-stacked device structure is sought, where the distance between the top and bottom electrodes can be regulated by controlling the thickness of the CQD film deposition.

7.2 Vertically-stacked barrier devices

Along with the improved charge collection efficiency, moving toward vertically-stacked design provides two key advantages. Firstly, it enables direct integration with silicon readout integrated circuits (ROICs) to create upward-looking focal plane arrays (FPAs), as shown in Fig. 10(a), thereby removing the fabrication complexity associated with hybridization.[90,91] Secondly, the design enables the incorporation of different functional layers inside the device via facile LBL fashion to realize various types of devices; this is a critical element for Ag_2Se intraband CQD devices since the CQD film is degenerately n-doped. In a vertical device, electrical conduction through a thin, heavily-doped CQD film (~ 300 nm) from the top to bottom electrodes, as opposed to a large 10 µm lateral conduction path

used in planar photoconductive devices,–makes the vertical device too conductive to measure any detector properties. A potential barrier can be introduced to reduce the electrical conductivity (in the dark). An ideal barrier structure that can minimize the dark conductivity would be the one that consists of both electron and hole barriers that can block thermally-generated electrons and holes respectively, while providing an unimpeded flow of photogenerated carriers (unipolar barriers[92]). A demonstration of hole barrier devices was reported by Hafiz et al.,[42] where PbS CQD – a standard interband semiconductor QD widely used in QD optoelectronics [93–95] – is used to readily form a hole potential barrier due to suitable energy level alignment Fig. 10(b)). When 5 nm PbS CQDs were used to form a barrier layer for 5.5 nm Ag_2Se CQDs (4.5 µm intraband peak), about an 8-fold reduction in dark conductivity was observed (Fig. 10(c)). The linearity of current-voltage (I-V) characteristic indicates that the barrier device operates as photoconductive devices, similar to the planar photoconductive device discussed in section 7.1, but engineered with reduced electrical conductivity *via* adopting unipolar barrier design.

The fabrication of barrier devices is identical to simply creating a vertically-stacked photoconductive Ag_2Se CQD devices via LBL deposition except with an inclusion of a PbS CQD layer in the middle of the stack that forms a hole transport barrier (Fig. 10(a)). The uniqueness of this device design is such that the inclusion of the barrier layer does not change the device's contact property since Ag electrodes are always in contact with the Ag_2Se CQDs. This greatly simplifies the device fabrication procedure and enables direct transition from rudimentary photoconductor devices to advanced heterojunction stack devices. The study conducted by Hafiz et al.[42] reveals that optimizing the EDT ligand-exchange time of Ag_2Se CQD film is a critical step in maximizing the device responsivity. A systematic study of ligand-exchange duration versus device infrared responsivity shows a narrow temporal window (Fig. 10(d)); as the ligand-exchange proceeds up to 60 seconds, the responsivity rapidly rises and falls where a peak is reached at 30 seconds. Beyond 60 seconds, the intraband absorbance greatly weakens due to the depopulation of electrons in $1S_e$ induced by excess EDT ligand exchange. A similar phenomenon was also observed in intraband HgSe.[96] On the other hand, below 5 seconds, the CQDs in the film are not sufficiently ligand-exchanged and hence are not electronically-coupled, leading to negligible responsivity.

Fig. 10(e) shows the spectral responsivity of the Ag_2Se/PbS/Ag_2Se CQD barrier device. Compared to the photoconductive devices, about two orders of magnitude improvement in the peak responsivity was observed and is mainly attributed to the shorter distance (300 nm) that the photogenerated carriers have to travel in vertical QD-stack devices, compared to the 10 µm transport gap in planar photoconductors. The ability to apply higher bias also contributed to improving the responsivity where the physical presence of the barrier layer helps to restrict the migration of silver ions. The measured responsivity of 13.3 mA/W (0.35V) at 4.5 µm peak corresponds to an EQE of 0.36 %. The low EQE is attributed to intrinsically low carrier hopping mobility which

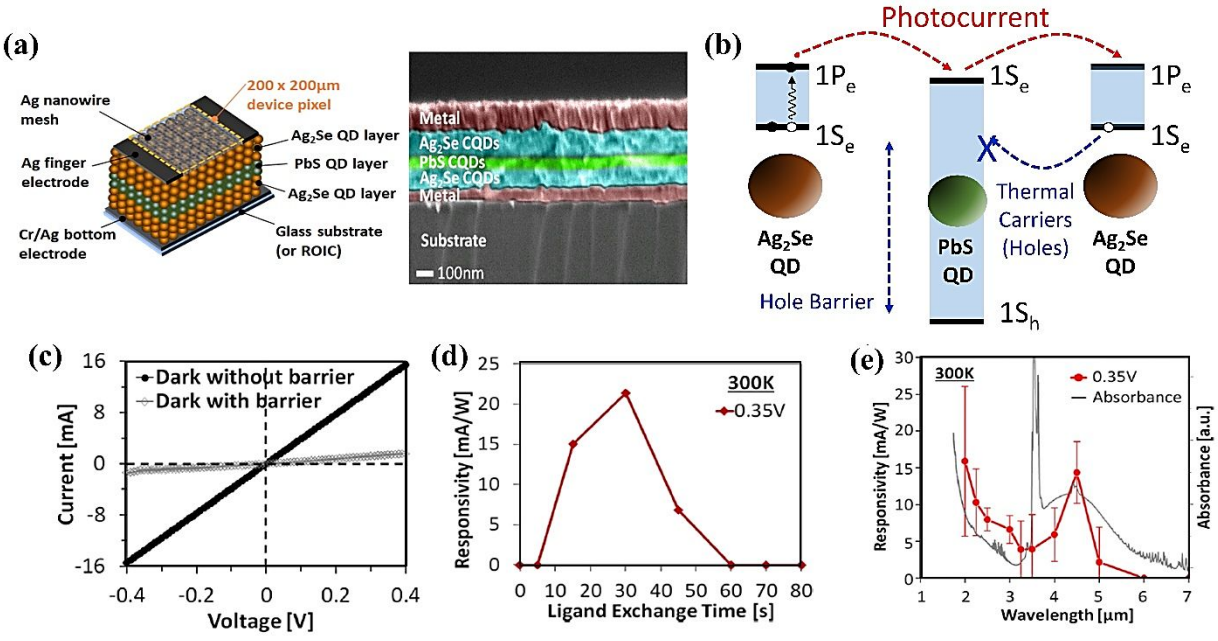

Fig. 10 (a) Schematic representation Ag_2Se/PbS/Ag_2Se CQD barrier device and the cross-sectional scanning electron microscopy (SEM) image[42]. (b) Energy level alignment between 5.5 nm Ag_2Se CQD and 5 nm PbS CQD. (c) I-V data obtained under dark from devices with barrier and without barrier layer,[42] (d) Responsivity at 4.5 µm, plotted as a function of EDT ligand exchange duration[42] (e) Spectral responsivity obtained from barrier device.[42] Copyright © 2020 American Chemical Society

degrades the charge collection efficiency and the limited thickness of Ag_2Se CQD absorber film. The thickness required to absorb 90 % of incoming MWIR radiation is in the order of several micrometers, whereas Ag_2Se CQD thickness employed here is only ~ 240 nm. The light absorption can be improved by employing various optical techniques such as plasmonic enhancement[97,98] or optical interference.[99]

The performance of the photodetector is characterized by specific detectivity (D^*), given as:

$$D^* = \frac{R\sqrt{AB}}{I_n} = \frac{R\sqrt{A}}{i_n}$$

where A is the detector area, B is the bandwidth, I_N is the noise current, i_n is the noise current density, and R is the responsivity. The i_n measured at 15 Hz with 1 Hz bandwidth was 10^{-9} A□Hz$^{-1/2}$ and the D^* was 3 × 10^5 Jones at room temperature. While the work demonstrates the efficacy of a hole barrier device, greater improvement in the dark conductivity, hence in i_n, is anticipated in the electron barrier device. However, the materials options for an electron barrier with a small ionization potential (≈ -4.3 eV) are scarce.

7.3 P-N junction diode devices

The device dark current, hence the associated current noise, can be further reduced using p-n junction diode design. In photoconductive and barrier devices discussed previously, the magnitude of the dark current is governed by the concentration of the majority carriers. In contrast, in a p-n junction diode under reverse biased operation, the dark current is fed by the minority carriers.[100] Since the concentration of minority carriers is orders of magnitude lower than the majority carriers in a semiconductor system (known as np product, $n \cdot p = n_i^2$, where n is the electron concentration, p is the hole concentration, and n_i is the intrinsic thermal carrier concentration which is a fixed quantity at a given temperature), the p-n junction diode is expected to exhibit significant reductions in the dark current and i_n.

When intraband Ag_2Se CQDs are used to construct p-n junction diode, a unique challenge arises. In a typical p-n junction photodiode design, the absorber layer is usually depleted (built-in bias formed) to maximize the charge collection efficiency of the photo-excited carriers generated within that layer. Using degenerately-doped n-type Ag_2Se CQDs absorbers, a strongly-doped p^+-semiconductor is thereby needed to deplete the Ag_2Se CQD layer. The basic semiconductor theory tells us that the width of the depletion region is inversely proportional to the carrier concentration. Hence, an extremely small depletion region will be created in the heavily-doped Ag_2Se CQD absorber layer and the photocarrier collection efficiency will be degraded. Also, in an electrical point of view, the device will consist of p^+-n^+ junction which will form a tunnel diode or Esaki diode,[101] that will exhibit high reverse-biased tunnelling current with weak rectifying characteristics.

The work reported by Hafiz et al.[102] introduces a unique approach to overcome this problem. The work creates a CQD mixture film, which consists of 3 nm PbS CQDs that have lower

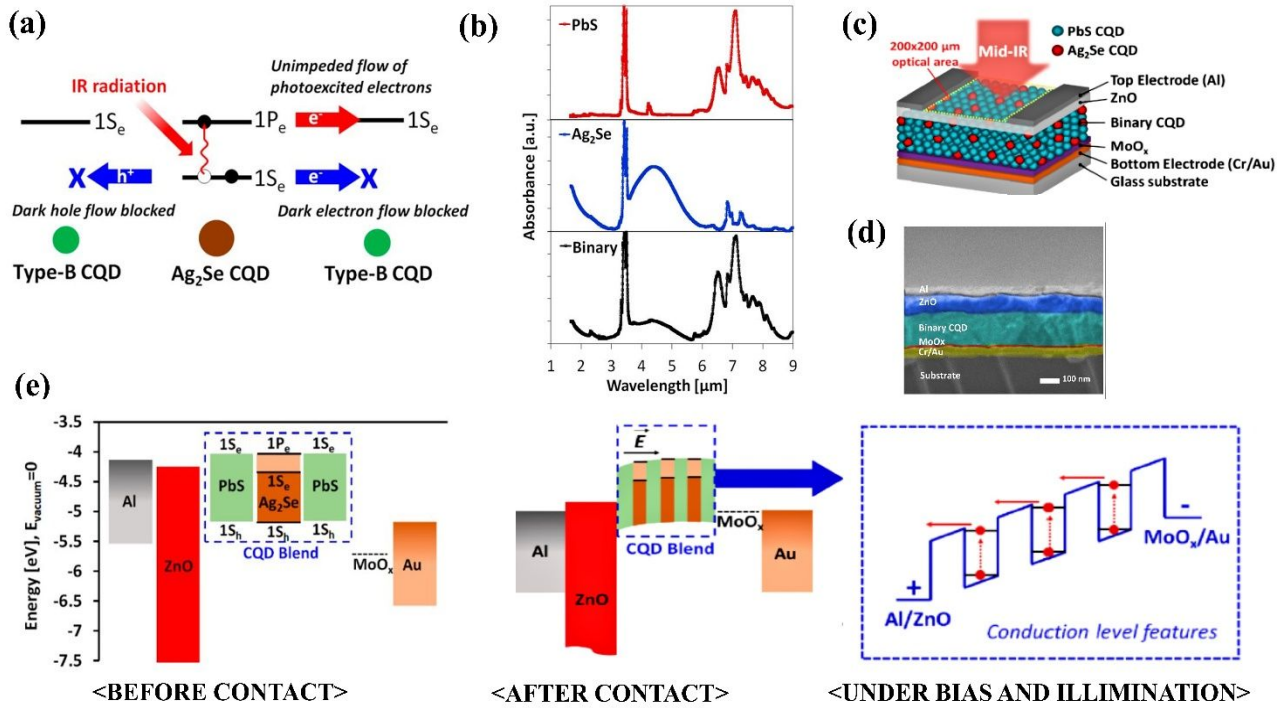

Fig. 11 (a) Schematic depicting the energy level alignment between Ag_2Se CQD and PbS CQD (type-B). (b) Optical absorbance spectrum obtained from pure PbS CQD film (top), pure Ag_2Se CQD film (middle) and binary mixture CQD film (bottom). (c) Schematic of binary CQD p-n junction device and (d) cross-sectional SEM of the device. (e) Energy level diagram of binary CQD device before contact (left), after contact (middle), and under bias and illumination (right).[102]

thermal carrier concentration (large interband gap) and 5.5 nm Ag_2Se CQDs that act as MWIR absorber-to realize rectifying p-n junction diodes. Compared to the pure Ag_2Se CQD film, when a binary mixture CQD is formed with PbS CQD being the major constituent of the film, the overall carrier concentration can be greatly reduced. The energy level alignment of the CQD mixture is depicted in Fig. 11(a). The large interband gap introduced by PbS CQDs imposes a transport barrier for ground-state electrons and holes thereby immobilizing them, evidenced by two-orders of magnitude reduction in the dark resistivity ($2 \times 10^5\ \Omega\cdot$cm), compared to the pure Ag_2Se CQD film ($1 \times 10^3\ \Omega\cdot$cm). This approach of mixing two different types of CQD to control the final electrical property of the film, is a strategy uniquely available in CQD material system. While the Ag_2Se CQDs now becomes a minor component and hence the MWIR absorption is reduced compared to the pure Ag_2Se CQD film, the peak arising from intraband absorbance of Ag_2Se CQD is still predominant in the mixture (at an optimized mixture ratio of 0.04, corresponding to 4 Ag_2Se CQD out of 100 PbS CQD), see Fig. 11(b). The binary mixture CQD film is p-type (since PbS CQD is the major constituent), as verified by Seebeck measurement, and the diode was constructed in junction with the ZnO, which serves as a n-type layer widely used in PbS CQD photovoltaic studies.[103]

The devices were fabricated by pre-patterning a Cr/Au electrode on a glass substrate using thermal evaporation and a shadow mask. Then a thin layer of MoO_x – a transport layer frequently used to improve the contact property of PbS CQDs[104,105] – was deposited. A binary PbS/Ag_2Se CQD layer was formed by LBL spin-casting (EDT ligand-exchanged) and ZnO nanoparticles were spin-casted on the top to form a p-n junction. The fabrication was completed by depositing Al top contact with two finger electrode that defines an optical window area of 200 × 200 µm, as shown in Fig. 11(c). The cross-sectional SEM of the device is shown in Fig. 11(d). The energy level diagrams before contact and after contact are illustrated in Fig. 11(d). Under the bias and illumination (Fig. 11(e)), photoexcited electrons generated from the Ag_2Se CQDs will cascade down toward the Al cathode, bearing a resemblance to the operation of epitaxial quantum dot infrared photodetectors (QDIPs).[106,107] A similar concept was demonstrated using HgSe intraband CQDs.[31]

A systematic device study on the CQD mixture ratio was conducted (Fig. 12(a)). With the increasing Ag_2Se CQD concentration, the device responsivity increased (due to an increase in the photoexcited electrons arising from Ag_2Se CQDs) and peaked at 0.04 mixture ratio. Further increase in the Ag_2Se CQD concentration, however, resulted in a decrease in the responsivity. A close examination of the diode parameters, extracted via fitting a standard diode equation,[108] reveals that reverse saturation current I_0 increases in orders of magnitude with increasing Ag_2Se CQD concentration. The magnitude of I_0 is indicative of how much carrier recombination is occurring inside the p-n junction device. This observation suggests that, with increasing Ag_2Se CQDs, recombination increases and later outweighs the enhancement in optical generation. Hence, the optimum mixture ratio that maximizes the responsivity is

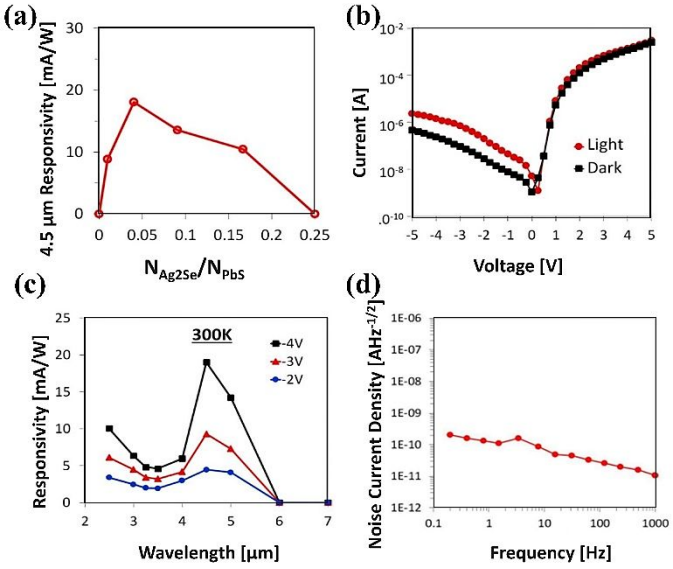

Fig. 12 (a) 4.5 µm device responsivity measured as a function of binary CQD mixture ratio. (b) I-V characteristics of binary CQD p-n junction device under dark and illumination. (c) Spectral responsivity of the device measured at different reverse biases. (d) Noise current density versus frequency plot obtained from the same device.[102] Copyright © 2021 American Chemical Society

determined to be 0.04. This observation leads to an important insight into future improvement for binary CQD devices, where identifying ligands with enhanced surface defect passivation would lead to higher optimum mixture ratio. Also, it was observed that, the device shunt resistance increases with increasing Ag_2Se CQDs. This is understood based on the fact that increasing the Ag_2Se CQD concentration inside the film increases the probability of creating direct percolation paths through the p-n junction; these are highly conductive paths since they consist of a path along n-type ZnO/n-type Ag_2Se CQD/metal contact.

Detector performance characterization was conducted on the device fabricated from optimized 0.04 mixture ratio. A strong rectifying, I-V characteristic with an on/off ratio of 7×10^3 and diode ideality factor of 3.2 was observed (Fig. 12(b)). Under illumination, a photovoltage corresponding to 250 mV was measured while, under reverse bias, a distinct photocurrent contribution to the diode current was observed. Spectral responsivities obtained under reverse biases (Fig. 12(c)) show peaks at 4.5 µm, which coincides with the optical absorption of the binary CQD film with the 4.5 µm intraband peak originating from Ag_2Se CQDs. The maximum responsivity of 19 mA/W was measured at a bias of -4 V. The smaller number of Ag_2Se CQDs present in the binary CQD devices allows higher biases to be applied, leading to higher responsivity values compared to the previous generation of barrier devices (15 mA/W, 0.35 V). Yet, due to the limited optical absorption and low carrier mobility of binary mixture CQD film, the EQE remains low (0.55 %). However, with a greater reduction in the dark current (several µA at -4V, compared to tens of mA at 0.4 V in barrier devices), 20-fold decrease in i_n of 4.91×10^{-11} A Hz$^{-1/2}$ was reported. The i_n as a function of frequency is plotted in Fig. 12(d). Up to 1 kHz, a clear 1/f trend was observed indicating that the flicker noise

is originate from the granular nature of the material and is independent of the chemical composition of the CQD material.[109] Overall, the device resulted in approximately an order of magnitude improvement in the D^* of 7.8 × 10^6 Jones at room temperature. The increase in the D^* is majorly due to improvement in the noise performance, an advantageous device property offered by reverse-biased p-n junction diodes.

8. Challenges and opportunities

Table 1 summarizes the current state-of-the-art and leading research CQD MWIR detector performances. For a single-pixel sensor devices, D^* is the main performance figure of merit that describes the device's ability to distinguish an incident optical signal from noise. For imaging FPAs, the primary performance parameter is the noise equivalent temperature difference (NETD) which is the temperature change of a scene required to produce a signal equal to the root mean square noise. In the MWIR, a minimum D^* of 2.15 × 10^9 Jones is required to operate the detector with NETD = 0.1 K for a staring imager with F# = 1 optics and operating with a standard frame rate of 50 frames per second.[110] InAsSb superlattice devices represent the state-of-the-art high-performance, cryogenically-cooled detector that achieves a D^* of 10^{12} Jones (cm·$Hz^{1/2}$/W) at 77K. However, note that when uncooled (300K), D^* of InAsSb superlattice device reduces to < 1.6 × 10^9 Jones. Microbolometer, a widely used option for low-cost, uncooled detector, performs with D^* of 10^8 - 10^9 Jones. This make bolometers useful for imaging in the LWIR (minimum D^* in LWIR is 0.65 x 10^8 Jones) but not in the MWIR [111] because the minimum D^* of 2.15 × 10^9 Jones is required. The current leading MWIR CQD detector research is based on interband HgTe CQD diode devices. While it performs favourably (D^* = 10^{11} Jones) with 100K cooling, D^* is limited to 10^8 Jones at room temperature.

For the intraband CQD devices, HgSe CQDs currently reports the highest D*. In a photoconductive device form, it reaches a D* of 10^8 at room temperature,[16] while diode devices report 1.5 x 10^9 at 80K.[31] Ag_2Se intraband CQDs, a non-toxic alternative to HgSe reports a room-temperature D* of 7.8 × 10^6 Jones based on the recent advancement on binary CQD p-n

Infrared Absorber material	Device Structure	Wavelength λ (μm)	Operating Temperature T (K)	Responsivity R (mA·W^{-1})	Noise Density i_n (A·$Hz^{-1/2}$)	Detectivity D^* (cm·$Hz^{1/2}$/W or Jones)	REF
InAsSb SL	Diode	4	77	1.5 × 10^3	1.8-7.3 × 10^{-15}	8.2 × 10^{12}	112,113
InAsSb SL	Diode	4.4	300	1.5-1.8 × 10^3	-	0.96-1.6 × 10^9	114
Bolometer	Thermal	9-13	300	1.4-1.5 × 10^7 V/W	-	0.83-2.3 × 10^9	115,116
HgTe CQDs (interband)	Photoconductor	4.8	85	230	1.0 × 10^{-13}	5.4 × 10^{10}	117
HgTe CQDs (interband)	diode	4.5	138	1620	0.07	4 × 10^{11}	118
HgTe CQDs (interband)	diode	3.8	100	420	5.9 × 10^{-14}	1.0 × 10^{11}	99
HgTe CQDs (interband)	diode	3.8	300	50	3.5 × 10^{-12}	2.0 × 10^8	99
HgSe CQDs (intraband)	Photoconductor	4.4	80	0.5	4.4 × 10^{-14}	8.5 × 10^8	12
HgSe CQDs (intraband)	Photoconductor	6	300	800	1 × 10^{-9}	~ 1.0 × 10^8	16
HgSe CQDs (intraband)	Photoconductor	5	80	0.13	1 × 10^{-12}	2.6 × 10^7	30
HgSe CQDs (intraband)	Photoconductor + resonator	4.4	80	3	-	1.0 × 10^9	119
HgSe CQDs (intraband)	Photoconductor	~4	80	77	~1 × 10^{-12}	1.7 × 10^9	120
HgSe CQDs (intraband)	Diode	4	80	5	~5 × 10^{-14}	1.0 × 10^9	31
HgSe CQDs (intraband)	Diode	4	200	6	-	2.0 × 10^8	120
HgSe CQDs (intraband)	CQDIP	4.4	80	0.1	1 × 10^{-13}	1.5 × 10^9	31
Ag_2Se CQDs (intraband)	Barrier device	4.5	300	13.3	1 × 10^{-9}	2.0 × 10^6	121

Table 1 Summary of current state-of-the-art and leading research MWIR detector performance parameters. SL denote superlattice.

Ag_2Se CQDs (intraband)	Diode	4.5	300	19	4.91×10^{-11}	7.8×10^{6}	102

p-n junction diode (photovoltaic) structure. Compared to the other CQD technologies, A good thermal infrared imager will operate with an NETD below 25 mK where the D^* lies in the range of 10^{11} Jones. If the intraband Ag_2Se CQD devices outperforms the current microbolometer technology and reach 10^{11} Jones, it may become a technologically viable option to fill the current MWIR gap. It is anticipated that improvements in D^* can be made by overcoming the following specific challenges:

(1) Optimal ligand identification: many CQD optoelectronics devices, as exemplified in the study of CQD solar cells,[122] report significant performance improvements through identifying better ligands than EDT (considered as standard organic ligand), which was used in all Ag_2Se devices to date. Although, there are prior preliminary studies on ligand variation in Ag_2Se CQD film, [80] ligands, such as TBAI atomic halide ligand, that works well with PbS CQD system do not necessarily translate into improved device performance in Ag_2Se CQDs. So far, for Ag_2Se CQDs, ligand that perform better than organic EDT has not been identified. Identifying ligands that can improve the carrier mobility-lifetime product[123] will directly impact the MWIR responsivity of the device.

(2) Controlled doping: in intraband CQDs, the need for controlled doping complicates the quest for identifying optimal ligands.[15,96] In Ag_2Se CQDs, electron doping of 2 electrons in $1S_e$ level is required to maximize the MWIR optical absorption. In the case of HgS intraband CQDs, a controlled doping that leads to MWIR absorbance enhancement/bleaching was demonstrated via introducing Hg^{2+} and S^{2-} surface absorbates.[124] The same strategy was reported to maximize the responsivity of HgSe CQD photoconductive devices recently.[110] In contrast, research efforts focused on controlling the $1S_e$ doping in Ag_2Se CQD is lacking. It is anticipated that controlled doping will lead to MWIR absorbance enhancement but also reduce the magnitude of the dark current since, completely filled $1S_e$ levels will lead to the scarcity of empty energy levels that ground electrons can hop to.[24]

(3) Noise reduction: in single crystalline semiconductors, shot noise or Johnson noise are typically the main contributors to noise. On the contrary, in CQD devices, a large 1/f noise is typically dominant over a wide range of frequencies,[125] and this is expected to be the ultimate performance limiting factor of the CQD device. However, a dedicated study on the noise performance of Ag_2Se intraband CQD is quite rare where CQD surface ligands, film morphology (ordering, cracks, and pinholes), and metal contacts can affect the magnitude of the 1/f noise. A systematic investigation on the device processing parameter versus noise performance relationship can shine a light on the future challenges and potentials of the Ag_2Se CQD-based MWIR devices.

(4) Material instability: the initial photoconductive device study showed that Ag_2Se CQD film is unstable at high bias (> 0.3 V), causing irreversible change to the device due to silver ion movement.[46] Compared, a typical interband PbS CQD photoconductor have demonstrated to withstand over 100 V bias.[126] Advancing the device structure to the barrier device and p-n junction diode, have lessen the bias instability problem. However, a materials-level solution can help improve the device long-term stability. Encapsulating Ag_2Se CQD with an ultra-thin shell[73] can be one of the strategies to overcome this issue.

9. Conclusions and outlook

CQD's are an important class of semiconductor material that can significantly reduce the cost of device manufacturing. Through wafer-scale solution processing, optoelectronic films can be deposited directly on top of existing electronic platforms, such as silicon read-out integrated circuits (ROICs). This heterogeneous integration can be achieved without the epitaxial and thermal constraints using CQDs. In the MWIR spectral regime, semiconductor absorbers that can be solution-processed are very rare, making intraband CQDs an important material option for low-cost infrared optoelectronics.

Among various intraband CQDs that are available today, Ag_2Se CQDs have demonstrated the most diverse device structural variations, from photoconductors to barrier devices and p-n junction diodes. These three major device structures examined in this article provide important understandings on the challenges and opportunities of Ag_2Se CQDs for MWIR sensors, which are critical for designing strategies toward future improvements.

Apart from the three major device structures examined in this review, there are more device designs that can be explored. One example is the multi-junction photovoltaic device where, in each junction, a thinner intraband CQD layer can be employed to overcome the CQD film's carrier diffusion length limitation and the improvements in the dark resistance with the increasing number of stacks can be exploited to lower the zero-bias resistance-area product (R_0A) and current noise. As a semiconductor CQD material with a unique benefit of low toxicity, continued research in advancing device structures and performances can solidify Ag_2Se intraband CQDs as a promising low SWAP-C alternative to current state-of-the-art epitaxial semiconductor devices.

While the intraband nature of Ag_2Se CQDs give rise to the Auger suppression property that can lead to high room temperature performance, its full potential has not yet been realized, hindered by a lack of research in CQD surface ligand chemistry, precise doping, and device noise performance. The successful outcomes generated from four future targeted studies discussed in the previous section 8, will directly contribute to the enhancement in the D^*, where the ultimate figure of merit goal lies in achieving 10^{11} Jones at room temperature.

As a further outlook, the impacts of the intraband CQD approach are not confined to lowering the cost of the conventional MWIR detector (single sensor or FPA) fabrication. This semiconductor CQD solution is amenable to high-resolution inkjet printing or large-area microscreen printing which removes the multiple masking steps required in conventional fabrication approaches. It is envisioned that the solution-processable intraband CQD technology discussed here may serve as a critical component to enabling digitized, additive manufacturing of future sensor arrays.[127]

Conflicts of interest

There are no conflicts to declare.

Acknowledgements

The authors thank US National Science Foundation (ECCS-1809112) for supporting various device studies presented in this review.

Notes and references

1 C. R. Kagan, L. C. Bassett, C. B. Murray and S. M. Thompson, *Chem. Rev.*, 2020, **121**, 3186–3233.
2 R. Paiella, *Intersubband transitions in quantum structures*, McGraw-Hill Education, New York, 2006.
3 D. Hofstetter, E. Baumann, F. R. Giorgetta, R. Théron, H. Wu, W. J. Schaff, J. Dawlaty, P. A. George, L. F. Eastman and F. Rana, *J. Phys. Condens. Matter*, 2009, **21**, 174208.
4 K.-K. Choi, B. F. Levine, C. G. Bethea, J. Walker and R. J. Malik, *Appl. Phys. Lett.*, 1987, **50**, 1814–1816.
5 H. C. Liu, J. Li, E. R. Brown, K. A. McIntosh, K. B. Nichols and M. J. Manfra, *Appl. Phys. Lett.*, 1995, **67**, 1594–1596.
6 J. Faist, F. Capasso, D. L. Sivco, C. Sirtori, A. L. Hutchinson and A. Y. Cho, *Science*, 1994, **264**, 553–556.
7 M. Beck, D. Hofstetter, T. Aellen, J. Faist, U. Oesterle, M. Ilegems, E. Gini and H. Melchior, *Science*, 2002, **295**, 301–305.
8 Y. Bai, S. R. Darvish, S. Slivken, W. Zhang, A. Evans, J. Nguyen and M. Razeghi, *Appl. Phys. Lett.*, 2008, **92**, 101105.
9 M. Rochat, L. Ajili, H. Willenberg, J. Faist, H. Beere, G. Davies, E. Linfield and D. Ritchie, *Appl. Phys. Lett.*, 2002, **81**, 1381–1383.
10 C. Walther, M. Fischer, G. Scalari, R. Terazzi, N. Hoyler and J. Faist, *Appl. Phys. Lett.*, 2007, **91**, 131122.
11 P. Guyot-Sionnest and M. A. Hines, *Appl. Phys. Lett.*, 1998, **72**, 686–688.
12 Z. Deng, K. S. Jeong and P. Guyot-Sionnest, *ACS nano*, 2014, **8**, 11707–11714.
13 Z. Deng and P. Guyot-Sionnest, *ACS nano*, 2016, **10**, 2121–2127.
14 M. Park, D. Choi, Y. Choi, H. Shin and K. S. Jeong, *ACS Photonics*, 2018, **5**, 1907–1911.
15 S. B. Hafiz, M. R. Scimeca, P. Zhao, I. J. Paredes, A. Sahu and D.-K. Ko, *ACS Appl. Nano Mater.*, 2019, **2**, 1631–1636.
16 E. Lhuillier, M. Scarafagio, P. Hease, B. Nadal, H. Aubin, X. Z. Xu, N. Lequeux, G. Patriarche, S. Ithurria and B. Dubertret, *Nano Lett.*, 2016, **16**, 1282–1286.
17 S. B. Hafiz, M. R. Scimeca, A. Sahu and D.-K. Ko, *ECS Trans.*, 2019, **92**, 11–15.
18 C. Melnychuk and P. Guyot-Sionnest, *ACS nano*, 2019, **13**, 10512–10519.
19 I. Ramiro, O. Özdemir, S. Christodoulou, S. Gupta, M. Dalmases, I. Torre and G. Konstantatos, *Nano Lett.*, 2020, **20**, 1003–1008.
20 M. R. Scimeca, N. Mattu, I. J. Paredes, M. N. Tran, S. J. Paul, E. S. Aydil and A. Sahu, *J. Phys. Chem. C*, 2021, **125**, 17556–17564.
21 A. Rogalski, *Rep. Prog. Phys.*, 2005, **68**, 2267.
22 D. Lee, M. Carmody, E. Piquette, P. Dreiske, A. Chen, A. Yulius, D. Edwall, S. Bhargava, M. Zandian and W. E. Tennant, *J. Electron. Mater.*, 2016, **45**, 4587–4595.
23 J. Qiu, Y. Liu, Z. Cai, Q. Phan and Z. Shi, *Mater. Adv.*, 2022, **3**, 1079–1086.
24 S. B. Hafiz, M. Scimeca, A. Sahu and D.-K. Ko, *Nano Converg.*, 2019, **6**, 7.
25 S. Becker, P. Imperinetti, J.-J. Yon, J.-L. Ouvrier-Buffet, V. Goudon, A. Hamelin, C. Vialle and A. Arnaud, *Proc. SPIE*, 2012, **8541**, 8541C.
26 J. J. Yon, E. Mottin, L. Biancardini, L. Letellier, and J. L. Tissot, in *Advanced Microsystems for Automotive Applications*, ed. J. Valldorf and W. Gessner, Springer, Berlin, Heidelberg, 2003, pp. 137–157.
27 A. Rogalski, *Infrared Physics & Technology*, 2011, **54**, 136–154.
28 M. E. Cryer and J. E. Halpert, *ACS Photonics*, 2018, **5**, 3009–3015.
29 C. Livache, B. Martinez, N. Goubet, J. Ramade and E. Lhuillier, *Front. Chem.*, 2018, **6**, 575.
30 M. Chen, G. Shen and P. Guyot-Sionnest, *J. Phys. Chem. C*, 2020, **124**, 16216–16221.
31 C. Livache, B. Martinez, N. Goubet, C. Gréboval, J. Qu, A. Chu, S. Royer, S. Ithurria, M. G. Silly and B. Dubertret, *Nat. Commun.*, 2019, **10**, 2125.
32 D.-K. Ko, in *2022 IEEE Research and Applications of Photonics in Defense Conference (RAPID)*, IEEE, Miramar Beach, FL, USA, 2022, pp. 1–2.
33 I. Ramiro, B. Kundu, M. Dalmases, O. Özdemir, M. Pedrosa and G. Konstantatos, *ACS nano*, 2020, **14**, 7161–7169.
34 P. Junod, H. Hediger, B. Kilchör and J. Wullschleger, *Philos. Mag.*, 1977, **36**, 941–958.
35 S. Huang, T.-R. Wei, H. Chen, J. Xiao, M. Zhu, K. Zhao and X. Shi, *ACS Appl. Mater. Interfaces*, 2021, **13**, 60192–60199.
36 Y.-P. Gu, R. Cui, Z.-L. Zhang, Z.-X. Xie and D.-W. Pang, *J. Am. Chem. Soc.*, 2012, **134**, 79–82.
37 J.-Y. Zhao, G. Chen, Y.-P. Gu, R. Cui, Z.-L. Zhang, Z.-L. Yu, B. Tang, Y.-F. Zhao and D.-W. Pang, *J. Am. Chem. Soc.*, 2016, **138**, 1893–1903.
38 D. Wang, T. Xie, Q. Peng and Y. Li, *J. Am. Chem. Soc.*, 2008, **130**, 4016–4022.
39 V. Buschmann, G. Van Tendeloo, P. Monnoyer and J. B. Nagy, *Langmuir*, 1998, **14**, 1528–1531.
40 A. Sahu, L. Qi, M. S. Kang, D. Deng and D. J. Norris, *J. Am. Chem. Soc.*, 2011, **133**, 6509–6512.
41 C. B. Murray, D. J. Norris and M. G. Bawendi, *J. Am. Chem. Soc.*, 1993, **115**, 8706–8715.
42 S. B. Hafiz, M. M. Al Mahfuz and D.-K. Ko, *ACS Appl. Mater. Interfaces*, 2021, **13**, 937–943.
43 C. M. Evans, M. E. Evans and T. D. Krauss, *J. Am. Chem. Soc.*, 2010, **132**, 10973–10975.
44 J. Son, D. Choi, M. Park, J. Kim and K. S. Jeong, *Nano Lett.*, 2020, **20**, 4985–4992.
45 R. Bera, D. Choi, Y. S. Jung, H. Song and K. S. Jeong, *J. Phys. Chem. Lett.*, 2022, **13**, 6138–6146.

46 H. Song, Y. Tischenko, D. Wasserman and K. S. Jeong, *Opt. Mater. Express*, 2023, **13**, 1328–1334.
47 C. Melnychuk and P. Guyot-Sionnest, *Chem. Rev.*, 2021, **121**, 2325–2372.
48 E. Lhuillier, T. H. Dang, M. Cavallo, C. Abadie, A. Khalili, J. C. Peterson and C. Gréboval, in *Handbook of II-VI Semiconductor-Based Sensors and Radiation Detectors*, ed. Ghenadii Korotcenkov, Springer, Cham, 2023, pp. 155–181.
49 R. Xie, Z. Li and X. Peng, *J. Am. Chem. Soc.*, 2009, **131**, 15457–15466.
50 I. Lignos, S. Stavrakis, A. Kilaj and A. J. deMello, *Small*, 2015, **11**, 4009–4017.
51 A. Shrestha, N. A. Spooner, S. Z. Qiao and S. Dai, *Phys. Chem. Chem. Phys.*, 2016, **18**, 14055–14062.
52 J. S. Owen, E. M. Chan, H. Liu and A. P. Alivisatos, *J. Am. Chem. Soc.*, 2010, **132**, 18206–18213.
53 R. W. Crisp, G. Grimaldi, L. De Trizio, W. H. Evers, N. Kirkwood, S. Kinge, L. Manna, L. D. Siebbeles and A. J. Houtepen, *Nanoscale*, 2018, **10**, 11110–11116.
54 J. Pan, A. O. El-Ballouli, L. Rollny, O. Voznyy, V. M. Burlakov, A. Goriely, E. H. Sargent and O. M. Bakr, *ACS nano*, 2013, **7**, 10158–10166.
55 C. Rivaux, T. Akdas, R. Yadav, O. El-Dahshan, D. Moodelly, W. L. Ling, D. Aldakov and P. Reiss, *J. Phys. Chem. C*, 2022, **126**, 20524–20534.
56 C.-C. Chen, A. B. Herhold, C. S. Johnson and A. P. Alivisatos, *Science*, 1997, **276**, 398–401.
57 J. M. McHale, A. Auroux, A. J. Perrotta and A. Navrotsky, *Science*, 1997, **277**, 788–791.
58 A. N. Goldstein, C. M. Echer and A. P. Alivisatos, *Science*, 1992, **256**, 1425–1427.
59 S. G. Kwon and T. Hyeon, *Acc. Chem. Res.*, 2008, **41**, 1696–1709.
60 C. Xiao, J. Xu, K. Li, J. Feng, J. Yang and Y. Xie, *J. Am. Chem. Soc.*, 2012, **134**, 4287–4293.
61 D. T. Schoen, C. Xie and Y. Cui, *J. Am. Chem. Soc.*, 2007, **129**, 4116–4117.
62 A. Sahu, D. Braga, O. Waser, M. S. Kang, D. Deng and D. J. Norris, *Nano Lett.*, 2014, **14**, 115–121.
63 A. Sahu, A. Khare, D. D. Deng and D. J. Norris, *Chem. Commun.*, 2012, **48**, 5458–5460.
64 J. Qu, N. Goubet, C. Livache, B. Martinez, D. Amelot, C. Gréboval, A. Chu, J. Ramade, H. Cruguel, S. Ithurria, M. G. Silly and E. Lhuillier, *J. Phys. Chem. C*, 2018, **122**, 18161–18167.
65 B. A. Tappan, B. Zhu, P. Cottingham, M. Mecklenburg, D. O. Scanlon and R. L. Brutchey, *Nano Lett.*, 2021, **21**, 5881–5887.
66 R. Makiura, T. Yonemura, T. Yamada, M. Yamauchi, R. Ikeda, H. Kitagawa, K. Kato and M. Takata, *Nat. Mater.*, 2009, **8**, 476–480.
67 J. Wang, K. Chen, M. Gong, B. Xu and Q. Yang, *Nano Lett.*, 2013, **13**, 3996–4000.
68 J. Wang, W. Fan, J. Yang, Z. Da, X. Yang, K. Chen, H. Yu and X. Cheng, *Chem. Mater.*, 2014, **26**, 5647–5653.
69 J. L. Wang, H. Feng and W. L. Fan, *Adv. Mater. Res.*, 2014, **850–851**, pp. 128–131.
70 D. H. Son, S. M. Hughes, Y. Yin and A. Paul Alivisatos, *Science*, 2004, **306**, 1009–1012.
71 S.-B. Wang, B. Hu, C.-C. Liu and S.-H. Yu, *J. Colloid Interface Sci.*, 2008, **325**, 351–355.
72 M. N. Kozicki, M. Mitkova, J. Zhu and M. Park, *Microelectron. Eng.*, 2002, **63**, 155–159.
73 M. Yarema, S. Pichler, M. Sytnyk, R. Seyrkammer, R. T. Lechner, G. Fritz-Popovski, D. Jarzab, K. Szendrei, R. Resel and O. Korovyanko, *ACS nano*, 2011, **5**, 3758–3765.
74 N. Graddage, J. Ouyang, J. Lu, T.-Y. Chu, Y. Zhang, Z. Li, X. Wu, P. R. Malenfant and Y. Tao, *ACS Appl. Nano Mater.*, 2020, **3**, 12209–12217.
75 C. Liao, L. Tang, L. Wang, Y. Li, J. Xu and Y. Jia, *Nanoscale*, 2020, **12**, 21879–21884.
76 A. M. Schimpf, N. Thakkar, C. E. Gunthardt, D. J. Masiello and D. R. Gamelin, *ACS nano*, 2014, **8**, 1065–1072.
77 G. Shen and P. Guyot-Sionnest, *J. Phys. Chem. C*, 2016, **120**, 11744–11753.
78 D. M. Kroupa, M. Vörös, N. P. Brawand, B. W. McNichols, E. M. Miller, J. Gu, A. J. Nozik, A. Sellinger, G. Galli and M. C. Beard, *Nat. Commun.*, 2017, **8**, 15257.
79 P. R. Brown, D. Kim, R. R. Lunt, N. Zhao, M. G. Bawendi, J. C. Grossman and V. Bulovic, *ACS nano*, 2014, **8**, 5863–5872.
80 S. B. Hafiz, M. M. Al Mahfuz, M. R. Scimeca, S. Lee, S. J. Oh, A. Sahu and D.-K. Ko, *Physica E Low Dimens. Syst. Nanostruct.*, 2020, **124**, 114223.
81 E. Lhuillier, S. Keuleyan and P. Guyot-Sionnest, *Nanotechnology*, 2012, **23**, 175705.
82 A. Rogalski, P. Martyniuk and M. Kopytko, *Prog. Quantum. Electron.*, 2019, **68**, 100228.
83 C. R. Kagan, E. Lifshitz, E. H. Sargent and D. V. Talapin, *Science*, 2016, **353**, aac5523.
84 Y. Liu, M. Gibbs, J. Puthussery, S. Gaik, R. Ihly, H. W. Hillhouse and M. Law, *Nano Lett.*, 2010, **10**, 1960–1969.
85 J. Jang, D. S. Dolzhnikov, W. Liu, S. Nam, M. Shim and D. V. Talapin, *Nano Lett.*, 2015, **15**, 6309–6317.
86 X. Lan, M. Chen, M. H. Hudson, V. Kamysbayev, Y. Wang, P. Guyot-Sionnest and D. V. Talapin, *Nat. Mater.*, 2020, **19**, 323–329.
87 S. E. Keuleyan, P. Guyot-Sionnest, C. Delerue and G. Allan, *ACS Nano*, 2014, **8**, 8676–8682.
88 A. Chu, C. Gréboval, Y. Prado, H. Majjad, C. Delerue, J.-F. Dayen, G. Vincent and E. Lhuillier, *Nat. Commun.*, 2021, **12**, 1794.
89 S. Ahn and O. Vazquez-Mena, *J. Chem. Phys.*, 2022, **156**, 024702.
90 E. J. Klem, C. Gregory, D. Temple and J. Lewis, *Proc. SPIE*, 2015, **9451**, pp. 17–21.
91 D. S. Temple, A. Hilton and E. J. Klem, *Proc. SPIE*, 2016, **9989**, pp. 57–63.
92 P. Martyniuk, M. Kopytko and A. Rogalski, *Opto-electron. Rev.*, 2014, **22**, 127–146.
93 R. Saran and R. J. Curry, *Nat. Photon.*, 2016, **10**, 81–92.
94 G. H. Carey, A. L. Abdelhady, Z. Ning, S. M. Thon, O. M. Bakr and E. H. Sargent, *Chem. Rev.*, 2015, **115**, 12732–12763.
95 S. Pradhan, F. Di Stasio, Y. Bi, S. Gupta, S. Christodoulou, A. Stavrinadis and G. Konstantatos, *Nat. Nanotechnol.*, 2019, **14**, 72–79.
96 A. Robin, C. Livache, S. Ithurria, E. Lacaze, B. Dubertret and E. Lhuillier, *ACS Appl. Mater. Interfaces*, 2016, **8**, 27122–27128.
97 Y. Yifat, M. Ackerman and P. Guyot-Sionnest, *Appl. Phys. Lett.*, 2017, **110**, 041106.
98 X. Tang, G. fu Wu and K. W. C. Lai, *J. Mater. Chem. C*, 2017, **5**, 362–369.
99 M. M. Ackerman, X. Tang and P. Guyot-Sionnest, *ACS nano*, 2018, **12**, 7264–7271.
100 B. G. Streetman and S. Banerjee, *Solid state electronic devices*, Prentice hall, Hoboken, New Jersey, 2000.
101 S. M. Sze, Y. Li and K. K. Ng, *Physics of semiconductor devices*, John wiley & sons, Hoboken, New Jersey, 2021.
102 S. B. Hafiz, M. M. Al Mahfuz, S. Lee and D.-K. Ko, *ACS Appl. Mater. Interfaces*, 2021, **13**, 49043–49049.
103 E. H. Sargent, *Nat. Photon.*, 2012, **6**, 133–135.

104 P. R. Brown, R. R. Lunt, N. Zhao, T. P. Osedach, D. D. Wanger, L.-Y. Chang, M. G. Bawendi and V. Bulović, *Nano Lett.*, 2011, **11**, 2955–2961.
105 J. Gao, C. L. Perkins, J. M. Luther, M. C. Hanna, H.-Y. Chen, O. E. Semonin, A. J. Nozik, R. J. Ellingson and M. C. Beard, *Nano Lett.*, 2011, **11**, 3263–3266.
106 Z. Ye, J. C. Campbell, Z. Chen, E.-T. Kim and A. Madhukar, *J. Appl. Phys.*, 2002, **92**, 7462–7468.
107 P. Martyniuk and A. Rogalski, *Prog. Quantum. Electron.*, 2008, **32**, 89–120.
108 E. Q. Macabebe and E. E. Van Dyk, *S. Afr. J. Sci.*, 2008, **104**, 401–404.
109 H. Liu, E. Lhuillier and P. Guyot-Sionnest, *J. Appl. Phys.*, 2014, **115**, 154309.
110 A. Khalili, M. Weis, S. G. Mizrahi, A. Chu, T. H. Dang, C. Abadie, C. Gréboval, C. Dabard, Y. Prado and X. Z. Xu, *ACS photonics*, 2022, **9**, 985–993.
111 J. Piotrowski and A. Rogalski, High-operating-temperature infrared photodetectors, SPIE press, Bellingham, 2007.
112 A. Haddadi, R. Chevallier, G. Chen, A. M. Hoang and M. Razeghi, *Appl. Phys. Lett.*, 2015, **106**, 011104.
113 A. Rogalski, P. Martyniuk, M. Kopytko, P. Madejczyk and S. Krishna, *Sensors*, 2020, **20**, 7047.
114 Teledyne Judson Technologies, https://www.teledynejudson.com/news/Documents/TJT%20SLS%20detector%20data%20charts%2009192017%20Final%2010131.pdf, (accessed April 2022).
115 A. Rogalski, *Opto-electron. Rev.*, 2010, **18**, 478–492.
116 A. Voshell, N. Dhar and M. M. Rana, Proc. SPIE, 2017, 10209, 92–107.
117 M. Chen, X. Lan, X. Tang, Y. Wang, M. H. Hudson, D. V. Talapin and P. Guyot-Sionnest, *ACS photonics*, 2019, **6**, 2358–2365.
118 X. Tang, M. M. Ackerman and P. Guyot-Sionnest, *ACS Nano*, 2018, **12**, 7362–7370.
119 A. Khalili, M. Cavallo, T. H. Dang, C. Dabard, H. Zhang, E. Bossavit, C. Abadie, Y. Prado, X. Z. Xu and S. Ithurria, *J. Chem. Phys.*, 2023, **158**, 094702.
120 M. Chen, Q. Hao, Y. Luo and X. Tang, *ACS Nano*, 2022, **16**, 11027–11035.
121 S. B. Hafiz, M. M. Al Mahfuz and D.-K. Ko, *ECS Trans.*, 2021, **102**, 45–51.
122 R. Wang, Y. Shang, P. Kanjanaboos, W. Zhou, Z. Ning and E. H. Sargent, *Energy Environ. Sci.*, 2016, **9**, 1130–1143.
123 K. S. Jeong, J. Tang, H. Liu, J. Kim, A. W. Schaefer, K. Kemp, L. Levina, X. Wang, S. Hoogland and R. Debnath, *ACS Nano*, 2012, **6**, 89–99.
124 K. S. Jeong, Z. Deng, S. Keuleyan, H. Liu and P. Guyot-Sionnest, *J. Phys. Chem. Lett.*, 2014, **5**, 1139–1143.
125 A. De Iacovo, C. Venettacci, L. Colace, L. Scopa and S. Foglia, *Appl. Phys. Lett.*, 2017, **111**, 211104.
126 G. Konstantatos, I. Howard, A. Fischer, S. Hoogland, J. Clifford, E. Klem, L. Levina and E. H. Sargent, *Nature*, 2006, **442**, 180–183.
127 J. Park, M. M. Al Mahfuz, R. Huebner and D.-K. Ko, *ACS Appl. Electron. Mater.*, 2023, **5**, 2386–2393.

Mohammad Mostafa Al Mahfuz *obtained his BS degree(2016) and MS Degree(2018) in Electrical and Electronics Engineering from University of Dhaka (Bangladesh). Currently, he is a PhD candidate in the Department of Electrical and Computer Engineering at New Jeresey Institute of Technology under the supervision of Prof. Dong-Kyun Ko. His current research interests include colloidal quantum dots, MWIR Detectors and thin film transistors.*

Junsung Park *is a post-doctoral research associate of Electrical and Computer Engineering at the New Jersey Institute of Technology. He received his Ph.D. degree in Electrical Engineering from Rensselaer Polytechnic Institute. His current research interest includes colloidal nanocrystals-based mid-wavelength infrared detectors.*

Rakina Islam *Rakina Islam is a graduate student of Electrical and Computer Engineering at the New Jersey Institute of Technology. She received her B.Sc degree in Electrical and Electronic Engineering from Islamic University of Technology. Her current research focus lies in lead chalcogenide-based CQDs. Her research interest also include CQD-based emitter devices.*

Dong-Kyun Ko *is an associate professor of Electrical and Computer Engineering at the New Jersey Institute of Technology. He received his Ph.D. degree in Materials Science and Engineering from University of Pennsylvania and held a postdoctoral position at Massachusetts Institute of Technology. He has over 15 years of experience in colloidal quantum dot electronics/optoelectronics research and served as lead symposium organizer for Quantum Dot Science and Technology Symposium at the Electrochemical Society (ECS) meetings as well as track chair of Nanoelectronic Devices at the IEEE International Conference on Nanotechnology (IEEE-NANO).*